Electron Thermal Microscopy

Todd Brintlinger,†,‡ Yi Qi,† Kamal H. Baloch,§ David Goldhaber-Gordon,‖ and John Cumings*,†,‖

Department of Materials Science and Engineering, Center for Nanophysics and Advanced Materials, Institute for Physical Sciences and Technology, University of Maryland, College Park, Maryland 20742, and Department of Physics, Stanford University, Stanford, California 94305

ABSTRACT

We present real-time, nanoscale temperature mapping using a transmission electron microscope and standard phase transitions in metal islands. Islands are deposited on the reverse side of commercially available silicon nitride membranes, while local thermal gradients are produced by Joule heating in a thin wire on the front side of the membrane. Change in contrast due to the liquid–solid transition in the islands allows the mapping of absolute temperature, as above or below the transition temperature, over the entire field-of-view. Experiments demonstrate nanoscale (<100 nm) resolution and video-rate (>30 thermal-images per second) speed, supported by combined electrical and thermal modeling. This provides a generic and adaptable platform for nanoscale thermal characterization independent of strong probe coupling and optical effects.

The progress of semiconductor electronics toward ever-smaller length scales and associated higher power densities brings a need for new high-resolution thermal microscopy techniques.[1,2] Traditional thermal microscopy is performed by detecting infrared radiation with far-field optics, where the resolution is limited by the wavelength of the light.[3] By adopting a serial, local-probe approach, near-field and scanned-probe microscopies can surpass this limit but sacrifice imaging speed.[4−15] In the same way that electron microscopy was invented to overcome the resolution limits of light microscopy,[16] we here demonstrate that an electron microscope can be used to overcome the limits of infrared thermal microscopy without compromising imaging speed. With this technique, which we call electron thermal microscopy, temperature is spatially resolved by observing the liquid−solid transition in arrays of nanoscale islands, producing thermal maps in real-time (30 thermal images per second over a 16 μm^2 field-of-view).

A key challenge in pushing thermal imaging to smaller length scales is generating reliable information about the local temperature. For instance, scanning thermal microscopy[17] infers the sample temperature from interfacial heat transfer, which then must be separately characterized due to its strong dependence on experimental details (e.g., thermal conductivities, probe shape, water meniscus, etc.). Near-field optical techniques[4] similarly must rely on a given surface evanescent

emissivity or characterize it separately. To provide a direct measure of temperature, we demonstrate that nanoscale metal islands can be used as passive local temperature probes. Observing phase transitions in an ensemble of islands gives a map of the absolute temperature relative to the transition point. These transitions can be standardized[18] and provide a reliable measure of the local thermodynamic temperature, by virtue of being connected to intrinsic equilibrium phase-phenomena. Furthermore, each island is sampling temperature simultaneously, allowing a parallel determination of temperature over the entire field-of-view. This is in distinction from serial techniques that require that the probe come to equilibrium at each point separately, making electron thermal microscopy inherently faster than any serial technique. This measurement platform is applicable to a variety of materials, is complementary to existing measurement techniques, and has potential for evaluating thermal management as devices scale down to lengths approaching characteristic scattering distances of thermal carriers, typically[19] 10−100 nm.

Figure 1 illustrates the principle underlying electron thermal microscopy.[20] Figure 1a depicts islands of a low-melting-point metal (here, indium) deposited using thermal evaporation in 2 × 10^{-6} Torr onto the back side of a 100 nm commercially available silicon nitride membrane window.[21] Using a specimen heating holder, the metal islands are heated through the melting transition in situ while imaging in a transmission electron microscope (see Supporting Information for details). Interestingly, the island shape does not change upon heating through the melting transition, owing to an oxide crust encasing each island.

* Corresponding author. E-mail: cumings@umd.edu.
† Department of Materials Science and Engineering, University of Maryland.
‡ Center for Nanophysics and Advanced Materials, University of Maryland.
§ Institute for Physical Sciences and Technology, University of Maryland.
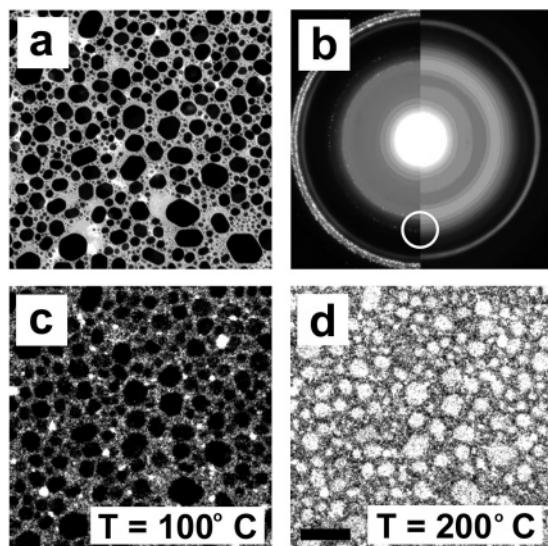‖ Stanford University.

Figure 1. Imaging liquid/solid-phase transitions in a transmission electron microscope. (a) A bright-field image of indium islands deposited on a silicon nitride membrane. (b) A composite diffraction pattern from indium islands in both liquid and solid phases. The white circle shows approximately where the objective aperture is placed for the dark-field images in panels c and d. (c,d) Dark-field images of same region with indium islands in the solid and liquid phases, respectively. Thus, each island acts as a local, binary temperature probe. Scale bar is 300 nm.

There is also no detectable change in contrast during melting when the islands are imaged in standard bright-field mode. However, the composite diffraction pattern shown in Figure 1b for both liquid and solid phases reveals a marked change in the diffraction properties of the islands between the two. Tilting the incident imaging beam so that the objective aperture is at the position indicated by the white circle in Figure 1b yields the dark-field images shown in Figure 1, panels c and d for the solid and liquid phases, respectively. In this imaging mode, the melting transition of each island is easily detectable as a change in the intensity at the location of the island. Therefore, it serves as a "binary" thermal-imaging technique with each metal dot reporting the local temperature as either above or below T_{melt}. The melting temperatures of the individual dots are all close to the bulk melting temperature of indium (156.6 °C), with a small amount of melting-point suppression (typically less than 10 °C), depending on the size and shape of the islands.[22] This suppression is more significant in smaller diameter islands and is limited in the present study by using only larger islands (>30 nm in-plane radius) for temperature determination. Upon cooling, the dots solidify once again at or below their initial melting temperature (see Supporting Information). These phenomena are in agreement with previous reports.[23,24] The metal is thus robust to thermal cycling and allows repeated temperature measurements of a given region.

Imaging this transition in many islands over a wide field-of-view, it is possible to study local temperature changes on the nonetched front side of the silicon nitride membrane, as is illustrated in Figure 2. To create local temperature gradients, metal heater wires were fabricated on the front side of the membranes and biased to create Joule heating. A

bright-field image of the device is shown in Figure 2a with tapered electrodes at top and bottom and a 54 nm wide, 870 nm long heater line spanning between them. Figure 2b is a thermal map derived from a series of thermal images, such as those in Figure 1c,d, applied to the region in Figure 2a. The color of each island is determined by the lowest heater current that causes it to melt; thus, areas of like color in the thermal image represent isothermal regions of the specimen. The hottest regions occur in the middle of the heater wire, as expected for Joule heating in standard Ohmic metal wires.

Figure 2c depicts finite-element analysis (FlexPDE, ver. 4.2) of the same region and using the same colors as Figure 2b. While Figure 2c only displays the area near the device, the full simulation is performed over the entire membrane window. In this model, temperature is given by

$$\nabla\cdot(K\nabla T) + P = 0 \tag{1}$$

where K is the local thermal conductivity, T is the temperature, and P is power, which is given by

$$P = \sigma|\nabla V|^2 \tag{2}$$

Here, V is the electric potential, and σ is the electrical conductivity. The temperature dependence of σ is given by

$$\sigma = \sigma_0\,(1 + \alpha\Delta T)^{-1} \tag{3}$$

where σ_0 is the room-temperature value and α is the temperature coefficient of resistivity. Potential and conductivity are governed by the steady-state equation

$$\nabla\cdot(\sigma\nabla V) = 0 \tag{4}$$

The edge of the silicon nitride membrane is treated as a fixed-temperature boundary condition at 22 °C, and voltage is applied to the electrode at the edge of the membrane. To test the model, we leave the thermal conductivity of the silicon nitride as a free parameter. The lowest voltage needed to initiate melting matches the experimental value when we set the modeled thermal conductivity of the silicon nitride to be $3.6^{+0.5}_{-0.1}$ W/m·K. (The asymmetric uncertainty stems from melting point suppression, as explained in the Supporting Information.) This value is then used to produce the thermal map shown in Figure 2c. Our inferred thermal conductivity agrees with previous measurements on free-standing amorphous silicon nitride membranes.[25−27]

The influence of the probe on the measurement is a potential concern for any thermal microscopy. For our new technique, the heating effect of the electron beam is easily quantified experimentally. Turning on the beam current for imaging typically adds 3.0 pA of current to the heater circuit. By reducing the temperature of the electron source, we can reduce the beam current by more than a factor of 30, so that this additional current falls below the noise level of our instrumentation (0.1 pA). At this reduced beam intensity, dark-field imaging is still possible, and the ensemble of
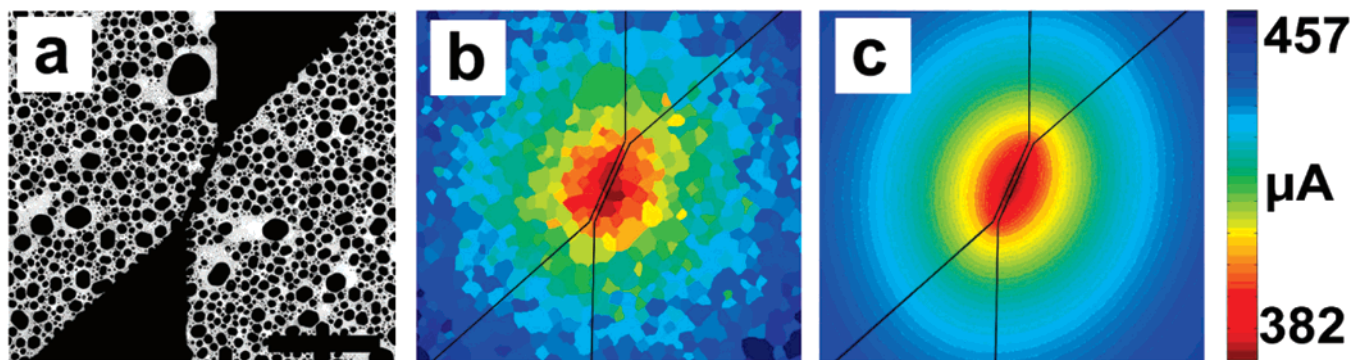
Figure 2. Demonstration of electron thermal microscopy. (a) A bright-field transmission electron micrograph of a heater wire with tapered electrodes fabricated on a silicon nitride membrane using electron-beam lithography. Application of bias to the electrodes allows nanoscale thermal gradients to be produced near the wire due to Joule heating. Indium islands are visible on the back side of the membrane. Scale bar is 1 μm. (b) A thermal map of the same region. Each pixel is colored according to the bias current needed to melt the indium island nearest to that pixel. The map is assembled from 50 separate images, recorded at increments of applied bias. (c) A finite-element thermal model of the device using a thermal conductivity of 3.6 W/m·K for the silicon nitride and a temperature coefficient of resistivity, α, of 1.8 $\times 10^{-3}$/K for palladium. Here, the colors represent currents that cause the regions to be greater than 157 °C, which is the melting temperature of bulk indium.
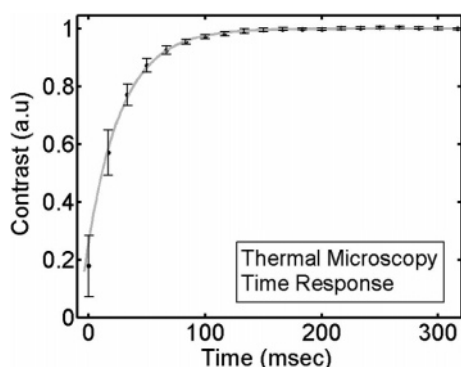

Figure 3. Time response of individual indium islands to a rapid temperature change. The y-axis indicates value assigned to contrast within a given indium island with 0 and 1 representing solid and liquid, respectively. The x-axis is time with $t = 0$ representing application of a voltage sufficient to melt all islands in field-of-view. Error bars show standard deviation over 14 different sets of images. Fitting (gray line) to asymptotic exponential decay yields a time constant 34 ± 2 ms, presumed to be limited by the video acquisition hardware.

indium islands systematically requires 1.0 ± 0.6 μW more Joule-heating power to melt than under conventional imaging conditions. This small amount of power is consistent with the amount that would be generated by 3.0 pA of current from a 300 kV imaging beam, suggesting that a majority of the beam-induced heating stems from high-momentum, high-loss scattering of the imaging electrons that eventually manifests itself as an electrical current in the electrodes. The beam-induced heating corresponds to a maximum of a few percent of the overall heating power used here, showing that our "probe" (imaging electron beam together with nanoscale metal islands) is quantifiably non-invasive.

In the demonstration, we also measure the time resolution. Figure 3 shows the time response of an ensemble of approximately 50 islands averaged over 14 repetitions of a step-function melting transition as imaged using video acquisition. At time $t = 0$, a bias large enough to melt all

islands in the field of view is applied to a heater wire such as that in Figure 2. The intensity of each island is then measured in each video frame. The y-axis of Figure 3 gives the average intensity as measured over all islands in the field of view with 0 and 1 representing the intensity of the solid and liquid phases, respectively. The step size along the x-axis corresponds to the 60 Hz acquisition rate in the video capture system. A fit yields an exponential time constant near 30 ms for a typical island. A thermal model based on a thermal diffusivity of silicon nitride of 0.025−0.25 cm²/s and a field-of-view of several microns suggests that the thermal response time of our sample to a step function of input power should be from 1 to 100 μs. Therefore, thermal diffusion is not rate determining in our thermal imaging, and the measured time response is probably limited by the image acquisition system. As alluded to previously, this time response is for a given island within the entire field-of-view. Separate islands respond this quickly but at spatially distinct points within a frame.

We now discuss the resolution limits of the technique, which are determined by the spacing of the metal islands and by the thickness of the dielectric membrane. Both limit the resolution in this practical demonstration to about 100 nm. However, thinner dielectric membranes are readily available, and smaller and more uniform diameter islands can be produced by maintaining higher substrate temperatures during metal deposition.[28] At these smaller sizes, melting point suppression would allow a spatial resolution of 30 nm together with a temperature precision of 10 °C, but this is not an absolute limit. Uniform metal islands with smaller diameters and homogeneous melting temperatures could instead be synthesized and deposited by chemical methods,[29] pushing the spatial resolution down to 10 nm or smaller without sacrificing temperature precision.

In summary, we present an electron-imaging technique that produces thermal maps with up to 16 μm² fields-of-view, video-rate acquisition, and a spatial resolution firmly in the

nanoscale range. We expect the technique to be useful as a method for observing heat generation, dissipation, and transport in a variety of nanoscale systems. While the demonstration utilizes a transmission electron microscope, which is only applicable to electron-transparent device geometries, preliminary results indicate that the technique can be readily adapted to scanning electron microscopy and back-scattered electron detection. Such thermal microscopy could be readily incorporated into routine device-characterization protocols for a broad range of relevant geometries.

Note Added in Proof: During review, we became aware of a similar manuscript describing a thermal microscopy platform based on the irreversible evaporation of gold nanoparticles.[30]

Supporting Information Available: Device fabrication and specimen holder, hysteretic behavior of islands during thermal cycling, α in the finite element model, and silicon nitride thermal conductivity and melting point suppression in the finite element model. This material is available free of charge via the Internet at http://pubs.acs.org.

References

(1) Cahill, D. G.; Ford, W. K.; Goodson, K. E.; Mahan, G. D.; Majumdar, A.; Maris, H. J.; Merlin, R.; Phillpot, S. R. Nanoscale thermal transport. *J. Appl. Phys.* **2003**, *93*, 793−818.

(2) International Technology Roadmap for Semiconductors 2005 edition. http:public.itrs.net (accessed May 5, 2007).

(3) Incropera, F. P.; DeWitt, D. P., *Fundamentals of heat and mass transfer*, 5th ed.; J. Wiley: New York, 2002; p xix, 981.

(4) Betzig, E.; Trautman, J. K. Near-Field Optics: Microscopy, Spectroscopy, and Surface Modification Beyond the Diffraction Limit. *Science* **1992**, *257*, 189−195.

(5) De Wilde, Y.; Formanek, F.; Carminati, R.; Gralak, B.; Lemoine, P.-A.; Joulain, K.; Mulet, J.-P.; Chen, Y.; Greffet, J.-J. Thermal radiation scanning tunnelling microscopy. *Nature* **2006**, *444*, 740−743.

(6) Crider, P. S.; Israeloff, N. E. Imaging Nanoscale Spatio-Temporal Thermal Fluctuations. *Nano Lett.* **2006**, *6*, 887−889.

(7) Edinger, K.; Gotszalk, T.; Rangelow, I. W. Novel high resolution scanning thermal probe. *J. Vac. Sci. Technol., B* **2001**, *19*, 2856−2860.

(8) Grabiec, P.; Radojewski, J.; Zaborowski, M.; Domanski, K.; Schenkel, T.; Rangelow, I. W. Batch fabricated scanning near field optical microscope/atomic force microscopy microprobe integrated with piezoresistive cantilever beam with highly reproducible focused ion beam micromachined aperture. *J. Vac. Sci. Technol., B* **2004**, *22*, 16−21.

(9) Hammiche, A.; Reading, M.; Pollock, H. M.; Song, M.; Hourston, D. J. Localized thermal analysis using a miniaturized resistive probe. *Rev. Sci. Instrum.* **1996**, *67*, 4268−4274.

(10) Kuball, M.; Hayes, J. M.; Uren, M. J.; Martin, I.; Birbeck, J. C. H.; Balmer, R. S.; Hughes, B. T. Measurement of temperature in active high-power AlGaN/GaN HFETs using Raman spectroscopy. *IEEE Electron Device Lett.* **2002**, *23*, 7−9.

(11) Majumdar, A. Scanning thermal microscopy. *Ann. Rev. Mater. Sci.* **1999**, *29*, 505−585.

(12) Nakayama, Y.; Pauzauskie, P. J.; Radenovic, A.; Onorato, R. M.; Saykally, R. J.; Liphardt, J.; Yang, P. Tunable nanowire nonlinear optical probe. *Nature* **2007**, *447*, 1098−1101.

(13) Nonnenmacher, M.; Wickramasinghe, H. K. Scanning Probe Microscopy of Thermal-Conductivity and Subsurface Properties. *Appl. Phys. Lett.* **1992**, *61*, 168−170.

(14) Olson, E. A.; Efremov, M. Y.; Kwan, A. T.; Lai, S.; Petrova, V.; Schiettekatte, F.; Warren, J. T.; Zhang, M.; Allen, L. H. Scanning calorimeter for nanoliter-scale liquid samples. *Appl. Phys. Lett.* **2000**, *77*, 2671−2673.

(15) Shi, L.; Majumdar, A. Recent developments in micro and nanoscale thermometry. *Microscale Thermophys. Eng.* **2001**, *5*, 251−265.

(16) Ruska, E. The Development of the Electron-Microscope and of Electron-Microscopy. *Rev. Mod. Phys.* **1987**, *59*, 627−638.

(17) Majumdar, A. Have we reached the limits of microscale thermometry? *Microscale Thermophys. Eng.* **1997**, *1*, 181−183.

(18) Preston-Thomas, H. The International Temperature Scale of 1990 (ITS-90). *Metrologia* **1990**, *27*, 3.

(19) Cahill, D. G.; Goodson, K.; Majumdar, A. Transactions of the Asme Thermometry and thermal transport in micro/nanoscale solid-state devices and structures. *J. Heat Transfer* **2002**, *124*, 223−241.

(20) Lereah, Y.; Deutscher, G.; Kofman, R. Evidence for Pre-Melting Surface Loosening of Lead Clusters Embedded in a Silicon Monoxide Matrix. *Europhys. Lett.* **1989**, *8*, 53−57.

(21) Membranes obtained from SPI company. http://www.2spi.com/. The membrane window is 500 μm square, and the silicon support frame is 200 μm thick and 2.6 mm square.

(22) Allen, G. L.; Bayles, R. A.; Gile, W. W.; Jesser, W. A. Small Particle Melting of Pure Metals. *Thin Solid Films* **1986**, *144*, 297−308.

(23) Blackman, M.; Sambles, J. R.; Peppiatt, S. J. Superheating of Bismuth. *Nature (London)-Phys. Sci.* **1972**, *239*, 61−62.

(24) Olson, E. A.; Efremov, M. Y.; Zhang, M.; Zhang, Z.; Allen, L. H. Size-dependent melting of Bi nanoparticles. *J. Appl. Phys.* **2005**, *97*, 034304.

(25) Holmes, W.; Gildemeister, J. M.; Richards, P. L.; Kotsubo, V. Measurements of thermal transport in low stress silicon nitride films. *Appl. Phys. Lett.* **1998**, *72*, 2250−2252.

(26) Lee, S. M.; Cahill, D. G. Heat transport in thin dielectric films. *J. Appl. Phys.* **1997**, *81*, 2590−2595.

(27) Mastrangelo, C. H.; Tai, Y. C.; Muller, R. S. Thermophysical Properties of Low-Residual Stress, Silicon-Rich, Lpcvd Silicon-Nitride Films. *Sens. Actuators, A* **1990**, *23*, 856−860.

(28) Wronski, C. R. M. Size Dependence of Melting Point of Small Particles of Tin. *Br. J. Appl. Phys.* **1967**, *18*, 1731−1737.

(29) Schmid, G. Large clusters and colloids. Metals in the embryonic state. *Chem. Rev.* **1992**, *92*, 1709−1727.

(30) Begtrup, G. E.; Ray, K. G.; Kessler, B. M.; Yuzvinsky, T. D.; Garcia, H.; Zettl, A. Probing nanoscale solids at thermal extremes. *Phys. Rev. Lett.* **2007**, *99*, 155901.

NL0729375